

ARTICLE OPEN



Dirac fermion metagratings in graphene

Pengcheng Wan¹, Yinghui Ren¹, Qianjing Wang¹, Di Huang¹, Ling Zhou¹, Haiqin Guo¹ and Junjie Du¹✉

We theoretically demonstrate a Dirac fermion metagrating which is an artificially engineered material in graphene. Although its physics mechanism is different from that of optical metagrating, both of them can deliver waves to one desired diffraction order. Here we design the metagrating as a linear array of bias-tunable quantum dots to engineer electron beams to travel along the -1st-order transmission direction with unity efficiency. Equivalently, electron waves are deflected by an arbitrary large-angle ranging from 90° to 180° by controlling the bias. The propagation direction changes abruptly without the necessity of a large transition distance. This effect is irrelevant to complete band gaps and thus the advantages of graphene with high mobility are not destroyed. This can be attributed to the whispering-gallery modes, which evolve with the angle of incidence to completely suppress the other diffraction orders supported by the metagrating and produce unity-efficiency beam deflection by enhancing the -1st transmitted diffraction order. The concept of Dirac fermion metagratings opens up a new paradigm in electron beam steering and could be applied to achieve two-dimensional electronic holography.

npj 2D Materials and Applications (2021)5:42; <https://doi.org/10.1038/s41699-021-00222-3>

INTRODUCTION

Graphene has emerged as a promising platform for developing alternative electronic devices with higher performance and even microelectronics because of its exceptional properties such as high intrinsic mobility, high electrical conductivity, and ballistic transport at micron scales under ambient temperatures¹. Great progress has been made in developing functional devices such as Dirac fermion microscopes, electron waveguides, splitters and inductors both theoretically^{2,3}, and experimentally^{4–9}. Graphene ballistic electrons bear a close analogy to light since they share a linear dispersion relation. This similarity has inspired the development of quantum electron optics in graphene by applying enlightening ideas in optics to two-dimensional materials. The behaviours of graphene electrons and light can be understood within the same theoretical framework^{10–12}, and similar phenomena^{13,14} can be observed experimentally. Over the past decades, metaoptics has attracted tremendous interest owing to the extraordinary phenomena that are not available in naturally occurring materials^{15–19}. Extending these manipulation methods to graphene is natural because it is a promising candidate for breaking the limitation of conventional electron manipulation methods, as has been done in optics. Negative refraction, a peculiar behaviour in optical metamaterials, has been reported in graphene theoretically²⁰ and experimentally^{21,22} with the demonstration of a Dirac fermion Veselago lens. However, metagratings for Dirac fermions have not yet been studied. Metagratings have exhibited great application potential in beam steering^{23–27} and metaholography^{28,29} by guiding light to the desired diffraction order. In this paper a Dirac fermion metagrating is illustrated with the extraordinary wave beam manipulation abilities, theoretically realized by a linear array of gate-bias-controlled quantum dots (QDs).

The metagrating channels electron waves into the -1st-order transmission direction and thus enables the arbitrary large-angle beam deflection. Steering electron beams to an arbitrary large deflection angle remains a challenge in graphene. This can be partly attributed to the Klein tunnelling which is one of the

characteristic features of ballistic electrons in graphene³⁰. Near-normal-incidence electrons can pass through arbitrarily high potential barriers with no damping by undergoing a transition between electron-like and hole-like states. This rules out all possibilities of reflecting electron waves at the near-normal incidence and hence hinders the large-angle deflection of reflected electron beams. Opening a complete bandgap, explored both in theory^{31–34} and experiments³⁵, is one of the options to break this limitation. However, one has to take on the risk of loss of high intrinsic mobility of electrons, which is an advantage of graphene over conventional semiconductor materials. Another option demonstrated experimentally is to manipulate electron waves at the neutrality point where the conductivity drops with a power-law temperature dependence³⁶. However, the operating bandwidth is restricted to only the Dirac point with the requirement of extremely low temperatures. In addition, a bent waveguide was proposed theoretically. Only when the deflection angle is below 120° can high-efficiency deflection be attainable³⁷. In addition to the limited deflection angle, a smooth and sufficiently long transition region is required in such a waveguide to ensure high transmission through the bends, which prevents downsizing of electron units. In contrast to these approaches, the metagrating steers electron beams without the requirement of opening a complete bandgap or extremely low temperatures and simultaneously caters to the desire for miniaturization.

The metagrating eliminates the dependency on reflection and produces abrupt changes in the electron propagation direction by transmission at a negative angle. This means that the transmitted wave lies on the same side of the normal as the incident wave. Compared with conventional reflection, negative transmission avoids the Klein tunnelling, which comes into play for reflection. This is achieved when the induced particular electron whispering-gallery modes (WGM) within the QDs under the strong inter-QD interaction focus the scattering fields of the QDs into the negative-transmission direction. Recently, electron WGMs in graphene has received special attention in experimental research^{38–42} on quasi-bound states where the electrons are predicted to be able to be

¹Key Laboratory of Polar Materials and Devices, Ministry of Education, School of Physics and Electronic Science, East China Normal University, Shanghai, China. ✉email: phyjunjie@gmail.com

trapped for a finite time^{43–46}. Unlike these works, we focus on their radiative properties. These WGMs do not radiate electrons in the ordinary and -1st-order reflection directions at the arbitrary incidence and thus enable perfect large-angle beam deflection along the -1st-order transmission direction.

RESULTS AND DISCUSSION

Perfect large-angle beam deflection

QDs are circular potential steps that can be tuned by applying a desired bias. The steps are smooth on the scale of the lattice constant of graphene such that the intervalley scattering is neglected and the low-energy electron dynamics can be described by the single-valley Hamiltonian^{46–52}

$$H = -i\nabla\sigma + V\Theta(R_s - r), \quad (1)$$

where $\Theta(R_s - r)$ is the Heaviside step function, R_s is the radius of the circular QD, V is the bias and $\sigma = (\sigma_x, \sigma_y)$ are Pauli matrices. We use reduced units with $\hbar = 1$ and a Fermi velocity $v_F = 1$. At the same time, the steps are sharp on the scale of the de Broglie wavelength. The transition of potentials from the background to the QDs occurs over a distance ΔR_s . This distance should be smaller than $0.5R_s$ to ensure that the scattering behaviour can be well approximated by the step function⁵³. The electron scattering problem of such a single QD can be rigorously calculated by the Mie scattering method^{46,51,52} which helps predict the excited WGMs in experiments⁵⁴. Strong inter-QD interactions may occur in a linear QD array and dramatically alter the WGMs and thus electron scattering behaviour of QDs. Consequently, the array produces negative transmission with the distribution probability of the scattered electrons concentrated primarily in the -1st-order transmission direction. The configuration of the linear array and the propagation of the electron wave are schematically shown in Fig. 1a, where the blue circular dots represent the QDs and the angle θ_{WA} is the angle made by the incident wave with the linear array. Figure 1b shows the phase diagram of the -1st-order transmittance versus the bias V applied on the QDs and the angle θ_{WA} in reduced units with fixed incident-electron energy $E = 0.8$. The QD radius is $R_s = 1$ and the quantities with dimensions of length, including the lattice constant and wavelength, are in units of R_s , namely, wavelength $\lambda = 2\pi R_s/0.8$ and lattice constant $d = \lambda/(2 \cos \theta_{WA})$. Note that the lattice constant varies with θ_{WA} (as in Figs. 1b and 2) such that the metagratings only support the zeroth and -1st diffraction orders, and simultaneously, the angle of transmission into the -1st diffraction order equals the angle of incidence. Thus once R_s is known in real units, the incident-electron energy in real units can be achieved by $E = 0.8\hbar v_F/R_s$.

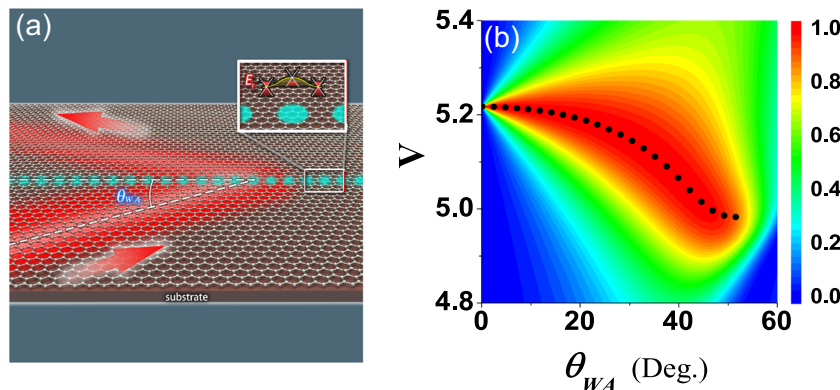


Fig. 1 The -1st-order transmittance. **a** Schematic view of the abrupt change in the propagation direction of the electron beam by a metagrating realized by a one-dimensional array of quantum dots on graphene. **b** Phase diagram of the -1st-order transmittance as a function of the bias applied on the QDs and angle θ_{WA} between the incident wave and the array. The calculation assumes QDs with radius $R_s = 1$ and incident energy $E = 0.8$, in reduced units. The bias V is controllable in practical applications. The black dotted line indicates unity efficiency.

Moreover, according to the definition of “refractive index” $N = (V - E)/E$, the bias is $V = (1 + N)E$. Our calculation for multiple QD systems exploits rigorous multiple-scattering theory^{12,55} (“Methods”), which takes into account the interaction between all the QDs, not just the neighbour interactions. By controlling the QD bias V , negative transmission with unity efficiency can be achieved for θ_{WA} ranging from 0° to 45° , which corresponds to a perfect wide-angle deflection from 90° to nearly 180° . Figure 2 presents the bending of Gaussian beams at three different angles θ_{WA} , simulated by using nanoscale QDs. Very recently, such nanoscale QDs with atomically sharp boundaries have been obtained in experiments^{56–58}. The fabrication techniques of high-precision QDs^{54,56–58} make it possible to demonstrate negative transmission in experiments.

The role of WGM in beam deflection

Obviously, the theory for bulk materials is not appropriate for a linear QD array. We thus have to turn our attention to individual QDs, which play a crucial role in negative transmission. To this end, we investigate the modes excited in a QD in the presence of other QDs. Due to the inter-QD coupling interaction, this case differs significantly from the case of an isolated QD. We use Mie scattering theory to analyse the modes because its expansion terms correspond one-to-one with the various modes. The scattered field is expressed as

$$\begin{aligned} \psi_s &= \begin{pmatrix} \psi_s^A \\ \psi_s^B \end{pmatrix} \\ &= \frac{1}{\sqrt{2}} \sum_{n=-\infty}^{+\infty} i^{n+1} a_n \begin{pmatrix} -iH_n^{(1)}(k_0 r) e^{in\phi} \\ \alpha H_{n+1}^{(1)}(k_0 r) e^{i(n+1)\phi} \end{pmatrix} \end{aligned} \quad (2)$$

where a_n is the scattering-field coefficient in the n th angular-momentum channel, α is the “band index”, and J_n and $H_n^{(1)}$ are the n th order Bessel function and Hankel function of the first kind, respectively. The band index in the background is $\alpha = \text{sgn}(E)$ and in the QD region is $\alpha' = \text{sgn}(E - V)$. Applying the reduced units, the wavenumbers in the two regions are $k_0 = \alpha E$ and $k_s = \alpha'(E - V)$. In this work, the QD radius is much less than the electron wavelength. The dominant scattering contributions come from the isotropic monopole, dipole, and quadrupole modes, corresponding to the terms $n=0$, $n=\pm 1$ and $n=\pm 2$, respectively.

For an isolated QD, the scattering coefficients follow $a_{-n} = a_{n-1}$ and $a_{-n} \neq a_n$. This is different from an isolated isotropic homogeneous dielectric rod in electromagnetism, for which $a_{-n} = a_n$. a_{-1} and a_1 correspond to clockwise and counterclockwise

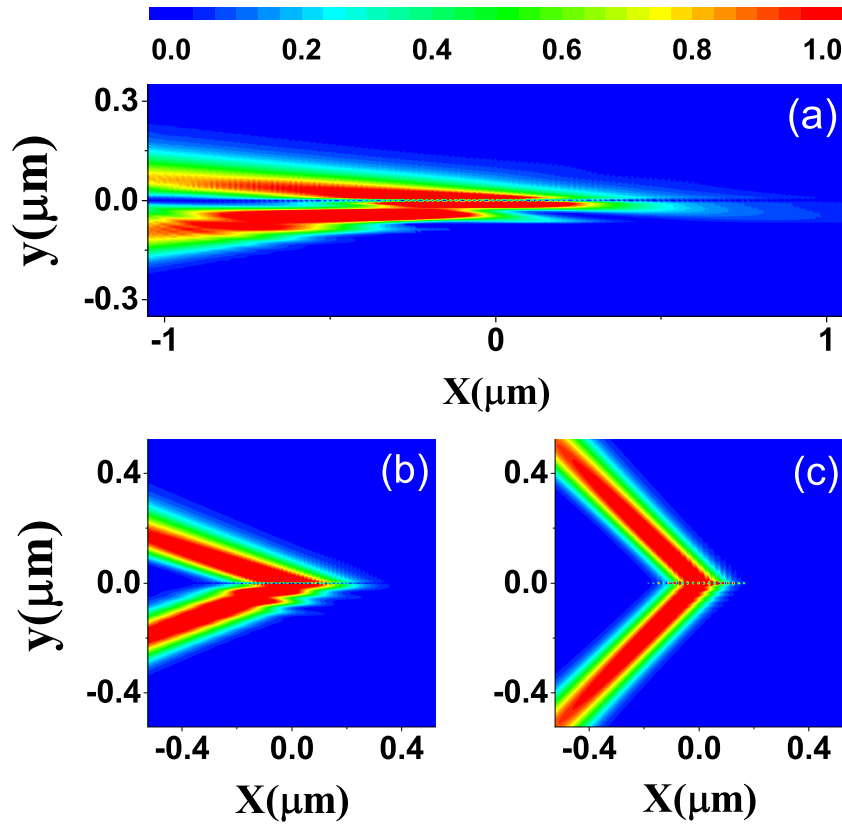


Fig. 2 Simulation of negative transmission. Negative-transmission-based deflection of electron beams at (a) $\theta_{WA} = 5^\circ$, (b) $\theta_{WA} = 20^\circ$, and (c) $\theta_{WA} = 45^\circ$. The bias and the lattice spacing are (a) $V = 977$ meV and $d = 14$ nm, (b) $V = 970$ meV and $d = 15$ nm, and (c) $V = 940$ meV and $d = 20$ nm. In all the cases, the QD radius is $R_s = 3.5$ nm and the incident electrons have a fixed energy $E = 148$ meV. The Gaussian beam has a waist radius $w = 3\lambda$.

circular dipole modes, respectively, and their interaction in a dielectric rod leads to a linear-oscillating dipole mode due to $a_{-1} = a_1$. Clearly, a linear dipole mode cannot be induced in an isolated QD. However, the inter-QD coupling significantly alters the symmetry of the scattering coefficients, with the relation $a_{-n} \neq a_{n-1}$. Figure 3 illustrates $|a_n|$ for a QD in an array for unity efficiency cases [black dotted line in Fig. 1b] at a deflection angle ranging from 90° to 180° . We can see that $a_1 = a_{-1}$ when $0^\circ < \theta_{WA} < 20^\circ$. Thus, the output will be a standard dipole mode. Meanwhile, the impact of the isotropic mode related to a_0 gradually increases with increasing θ_{WA} , although, its contribution is much less than that of the dipole mode for $\theta_{WA} < 20^\circ$. The coefficient a_{-2} , which represents a quadrupole mode, is nearly zero for $\theta_{WA} < 20^\circ$. As a result, the total scattering field from a QD in the linear QD array, calculated on a circle of radius $\rho = 60$ and in a square region at $\theta_{WA} = 5^\circ$ (20°), exhibits clear linear-oscillating dipolar characteristics [see Fig. 4a, b (Fig. 4c, d), respectively].

However, even though the linear dipole mode excited at $\theta_{WA} = 5^\circ$ is nearly standard, with $a_{-1} = a_1$, its radiation is not ordinary. First, it propagates transversely to the incident wave. However, in electromagnetism, it generally propagates parallel to the incident direction. Second, its radiation field has a definite and interesting phase relation with the radiation field obtained from the isotropic mode. The comparison between Fig. 5a, b shows that the scattering components of both modes are in phase and strengthen each other on the transmission side, whereas they are out of phase and interfere destructively on the reflection side. Accordingly, the total scattering probability is enhanced and spans the entire transmission region. However, it becomes weaker and more confined to the centre of the reflection region as θ_{WA} increases. Although the radiation from the isotropic mode is much

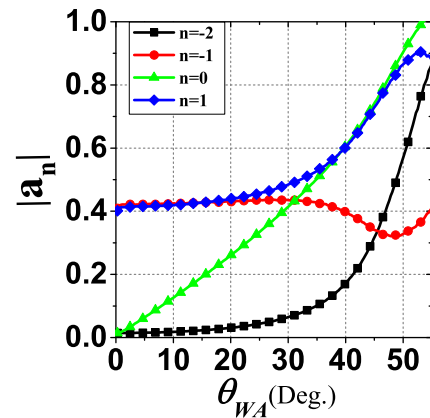


Fig. 3 Contribution from different multipole modes. Scattering coefficients of a QD for the four dominant angular-momentum channels as a function of θ_{WA} . The contribution from other angular momentum channels is negligible. The channels $n = -2$, $n = -1$ ($n = 1$) and $n = 0$ correspond to circular quadrupole, circular dipole, and isotropic modes, respectively. The QD is located in a linear array and inter-QD coupling is considered.

weaker than that from the linear dipole mode, the superposition of them makes the total scattering probability zero, especially in the directions of the ordinary and -1st-order reflection indicated in Fig. 4a, c by arrows R_0 and R_{-1} , respectively. The null scattering probability in the two directions at $\theta_{WA} = 5^\circ$ is also explicitly illustrated in Supplementary Fig. 1 in Supplementary Note 1. As a result, the ordinary and -1st-order reflections do not appear

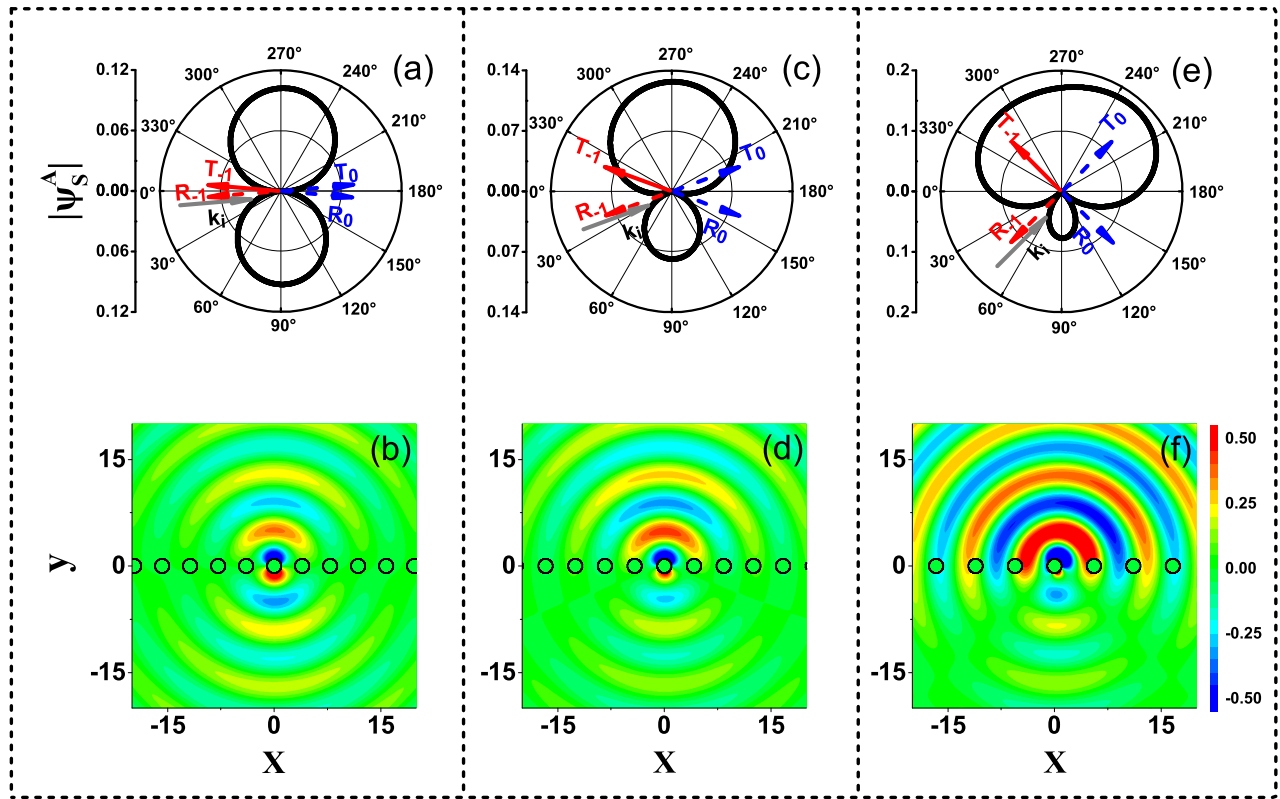


Fig. 4 Scattering from a QD in a linear array. **a** $|\text{Re}\{\psi_s^A\}|$ around a circle with radius $\rho = 60$, and **(b)** $\text{Re}\{\psi_s^A\}$ in a square region for $\theta_{WA} = 5^\circ$. $\text{Re}\{\psi_s^A\}$ is the real part of the first spinor component [see Eq. (2)] of the field scattered by a QD located in the linear array. **c**, **d** [(**e**) and (**f**)] correspond to $\theta_{WA} = 20^\circ$ ($\theta_{WA} = 45^\circ$). In the ordinary and -1st-order reflection directions, $\text{Re}\{\psi_s^A\}$ is zero, which leads to the disappearance of the two diffraction orders. This is also the case at $\theta_{WA} = 5^\circ$ (see Supplementary Fig. 1). The scattered fields are calculated for the QD located at the origin of the coordinates. The presence of many QDs in (**b**), (**d**) and (**f**) implies that inter-QD coupling has been considered.

because they arise from the interference between scattering from all QDs.

When $\theta_{WA} > 20^\circ$, a_0 and a_{-2} begin to play more important roles. At $\theta_{WA} = 45^\circ$, the scattering on the reflection side remains well suppressed, and the scattering probability nearly vanishes, as shown in Fig. 4e, f. This can be understood as resulting from the interaction between the four modes. Considering that $|a_{-2}|$ is nearly equal to $|a_{-1}|$, as are $|a_0|$ and $|a_1|$, at $\theta_{WA} = 45^\circ$, as shown in Fig. 3, we give the scattering contributed by a_{-2} and a_{-1} in Fig. 5c and that by a_0 and a_1 in Fig. 5d. The phases of the fields in Fig. 5c, d are compared at two points selected arbitrarily in the ordinary and -1st-order reflection directions. This figure shows that they are always out of phase and have nearly the same amplitude and thus will interfere destructively with each other, which means that the ordinary and -1st-order reflections are not supported by the linear array. Consequently, the metagrating does not support the ordinary and -1st-order reflection for arbitrary θ_{WA} between 0° and 45° .

Moreover, the propagation probabilities in the ordinary transmission direction are also inhibited in this range of incident angles. The ordinary transmission is the superposition of the incident wave and the total scattered wave and differs from the diffraction in all the other diffraction orders, which are only determined by the total scattered wave. The null propagation probability in this direction arises from the destructive interference owing to the opposite phases of the incident and scattered waves (see Supplementary Fig. 2 in Supplementary Note 2). Consequently, neither ordinary reflection and transmission nor -1st-order reflection are supported by the metagrating. Therefore, the unique nonzero propagation probability appears in the -1st-

order transmission direction. This leads to negative transmission and large-angle deflection of the incident electron beam.

Despite the details of the interaction between the four scattering coefficients, direct and deep insight into the beam deflection can be gained from the resultant WGMs within the QDs. As shown in Fig. 4b, d, f, the WGM is similar to a standard dipole when θ_{WA} approaches zero, then becomes asymmetric with increasing θ_{WA} , and finally turns into a rainbow-like mode near 45° . For the cases of near-zero θ_{WA} , the standard dipole mode in Fig. 4b does not radiate electrons into the ordinary and -1st-order reflection directions which are nearly parallel to the linear array. The WGM evolves into a rainbow-like mode on the transmission side, completely suppressing the radiation on the reflection side, near 45° , although the two reflected diffraction orders are very close to the vertical line of the particle array. Meanwhile, the WGMs can always give rise to radiation into the ordinary transmitted order, which is out of phase with the incident wave and these waves cancel each other at arbitrary incidence. The WGMs produce full inhibition of the other diffraction orders and enable the metagrating to realize perfect negative transmission into the -1st transmitted diffraction order. This implies that the WGMs, the localized nature of the metagrating, are the underlying physics behind the negative transmission. In addition, what WGMs are excited in the scattering process depends on the dimension of the QDs, the applied bias, the spacing and the wavelength, not on the shape of the QDs. Therefore it is not necessary to fabricate circular QDs in experiments. A striking example is that negative transmission has been obtained not only by circular rods but also by square rods in optics¹⁷. Negative transmission is also to some extent robust against the structure disorder (see Supplementary Fig. 3 in Supplementary Note 3).

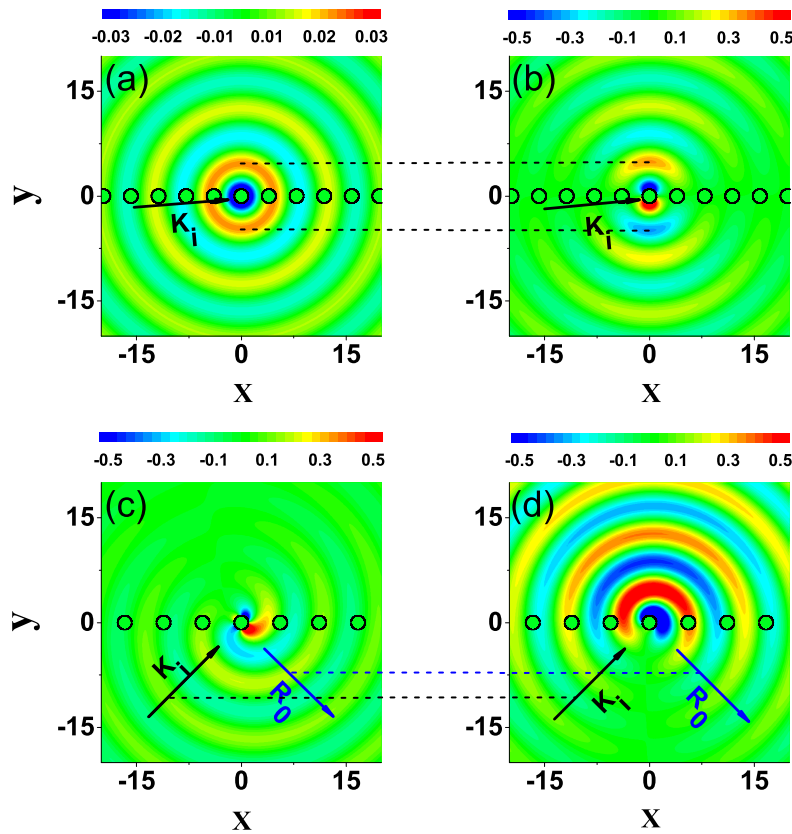


Fig. 5 Elimination of the ordinary and -1st-order reflections at $\theta_{WA} = 5^\circ$ and 45° . The scattered field distribution contributed (a) by the channel $n = 0$ corresponding to an isotropic mode and (b) by the channels $n = -1$ and 1 corresponding to a standard dipole mode at $\theta_{WA} = 5^\circ$. The scattered field distribution contributed (c) by the channels $n = -2$ and -1 and (d) by the channels $n = 0$ and 1 at $\theta_{WA} = 45^\circ$. The calculation is performed for the same QD with the inter-QD interaction considered as in Fig. 4. K_i and R_0 denote the incident and ordinary reflection directions, respectively.

Merits of metagrating-based beam deflection

Note that we actually obtain sharp changes in the direction of electron propagation by using the metagrating. First, the linear QD array is only one-QD-diameter thick, which is less than the electron wavelength. In Fig. 2, the wavelength of electrons (27.9 nm) is nearly four times the diameter ($2R_s = 7$ nm) of the QDs. Second, the transition distance necessary for high transmission (a larger bend radius than the wavelength) in bent waveguides becomes dispensable since the electron beam is bent immediately after passing through the QD array. In addition, the opening of a bandgap in graphene requires a structure thicker than the wavelength. Therefore, we use a subwavelength structure to realize the bending of electron waves. The electron beam indeed undergoes a drastic change in the propagation direction, namely, a sharp bend.

In the simulation, we assumed that graphene is suspended in a vacuum or air. In actual experiments, graphene is usually supported on a substrate, and the impacts of the substrate on the electrical properties of graphene must be considered. Therefore, we should give preference to the substrate that has as little impact as possible on graphene mobility. To this end, a substrate with a larger dielectric constant, such as HfO_2 , is preferred.

In summary, we illustrate a Dirac fermion metagrating that enables the deflection of electron beams in graphene at a near- 180° angle with unity efficiency by engineering the incident electrons into the -1st-order transmission direction. The mechanism based on transmission rather than reflection breaks the restriction of Klein tunnelling and avoids the possible loss of the high intrinsic mobility of electrons in graphene due to the opening of a complete bandgap. The extraordinary capabilities of

the linear arrays benefit from the excitation of various whispering gallery modes. The deflection occurs over a distance much smaller than electron wavelengths and no transition distance is required. Such an approach may be used to fabricate compact graphene devices with dramatically improved integration based on the abrupt change in the propagation direction. The one-dimensional design also allows precise control over the performance of individual QDs and the spacing between them. Finally, by controlling the bias applied to the QDs, unity efficiency can be ensured for a wide range of deflection angles.

METHODS

Mie scattering method

Firstly, we solve the scattering problem of a single gate-controlled QD based on Mie scattering method in graphene^{46,51,52}. The incident and scattered waves are expanded as follows:

$$\psi_{in} = \frac{1}{\sqrt{2}} \sum_{m=-\infty}^{+\infty} i^{m+1} \begin{pmatrix} -ip_m^A J_m(k_0 r) e^{im\phi} \\ ap_m^B J_{m+1}(k_0 r) e^{i(m+1)\phi} \end{pmatrix}, \quad (3)$$

$$\psi_s = \frac{1}{\sqrt{2}} \sum_{m=-\infty}^{+\infty} a_m i^{m+1} \begin{pmatrix} -iH_m^{(1)}(k_0 r) e^{im\phi} \\ aH_{m+1}^{(1)}(k_0 r) e^{i(m+1)\phi} \end{pmatrix}, \quad (4)$$

where m is an integer angular momentum quantum number, $p_m^A = e^{-i(m+\frac{1}{2})\phi_{inc}}$, $p_m^B = e^{-i(m-\frac{1}{2})\phi_{inc}}$, J_m and $H_m^{(1)}$ are, respectively, the m th order Bessel function and Hankel function of the first kind, ϕ_{inc} is the incident angle. Similarly, the inner field inside the dot can be written as

$$\psi^{ins} = \frac{1}{\sqrt{2}} \sum_{m=-\infty}^{+\infty} d_m i^{m+1} \begin{pmatrix} -iJ_m(k_s r) e^{im\phi} \\ \alpha J_{m+1}(k_s r) e^{i(m+1)\phi} \end{pmatrix}, \quad (5)$$

where k_0 and k_s are respectively the wave vector in the background region and the QD, the index $a = 1$ represents the conduction band and $a' = -1$ represents the valence band, and $k_s = Nk_0$ with the refractive index $N = |V - E|/E$. After imposing the boundary condition at the surface of the QD with its radius R_s , the size parameter $\rho = k_0 R_s$ is introduced and the scattering coefficient a_m is given

$$a_m = -\frac{J_m(\rho)J_{m+1}(N\rho)p_m^A - \alpha a' J_{m+1}(\rho)J_m(N\rho)p_m^B}{J_{m+1}(N\rho)H_m^{(1)}(\rho) - \alpha a' J_m(N\rho)H_{m+1}^{(1)}(\rho)}, \quad (6)$$

$$a_{-m} = -\frac{J_m(\rho)J_{m-1}(N\rho)p_{-m}^A - \alpha a' J_{m-1}(\rho)J_m(N\rho)p_{-m}^B}{J_{m-1}(N\rho)H_m^{(1)}(\rho) - \alpha a' J_m(N\rho)H_{m-1}^{(1)}(\rho)}. \quad (7)$$

The relation between the scattering coefficients a and the incident coefficients $\begin{pmatrix} p^A \\ p^B \end{pmatrix}$ in Eqs. (6) and (7) can also be expressed as $a = Sp$ by a scattering matrix S .

Multiple scattering method

In a linear QD array, the incident wave that strikes the surface of QD j consists of two parts: (1) the initial incident wave $\psi_{inc}^0(j)$ and (2) the scattered waves of all other QDs according to multiple scattering theory^{12,55} (also known in solid-state physics as the K.K.R. method^{59,60}). Thus it can be written as

$$\psi_{inc}(j) = \psi_{inc}^0(j) + \sum_{l \neq j} \psi_s(l). \quad (8)$$

By the translational addition theorem, the scattered wave from any other potential l (with $l \neq j$) can be expanded as follows,

$$\begin{aligned} \psi_s(l) &= \frac{1}{\sqrt{2}} \sum_{n=-\infty}^{+\infty} a_n^{(l)} r^{n+1} \begin{pmatrix} -iH_n^{(1)}(k_0 r) e^{in\phi} \\ aH_{n+1}^{(1)}(k_0 r) e^{i(n+1)\phi} \end{pmatrix} \\ &= \frac{1}{\sqrt{2}} \sum_{m=-\infty}^{+\infty} r^{m+1} \begin{pmatrix} -ip_m^{(lj)} J_m(k_0 r) e^{im\phi} \\ ap_m^{(lj)} J_{m+1}(k_0 r) e^{i(m+1)\phi} \end{pmatrix}, \end{aligned} \quad (9)$$

where

$$p_m^{(lj)} = \sum_n j^{(m-n)} H_{m-n}^{(1)}(kd_{lj}) e^{-i(m-n)\phi_{lj}} a_n^{(l)}, \quad (10)$$

and $\mathbf{d}_{lj} = d_{lj} \cos \phi_{lj} \hat{e}_x + d_{lj} \sin \phi_{lj} \hat{e}_y$ is the vector extending from the centre of QD l to that of QD j . In the main text, the linear QD array is placed along the x axis, so the angle θ_{WA} between the incident wave and the array equals the angle of incidence ϕ_{inc} .

Substituting (9) into Eq. (6) and $a^{(j)} = Sp^{(j)}$, one will yield a set of linear equations that contains the iterative scattering coefficients. In our practical numerical calculation, the series expansion was truncated at some $n = n_c$. With the equations, we can compute the scattering field at any position and the transmittance (reflectivity) of any order diffraction wave. To ensure the accuracy of the results in our paper, the minimum n_c should be larger than 2. Physically, the minimum n_c is determined by the wavelength, the radius of the QD and the bias voltage applied to the QD. The larger the ratio of the radius to wavelength or the bias voltage is, the larger the minimum n_c is.

In a linear QD array placed along the x direction, the transmittance in the v th transmitted order can be expressed as

$$T_v = |t_v|^2 = \left| \frac{2a_m^{(0)}}{dk_{yv}} \sum_{m=-\infty}^{+\infty} \frac{(k_{xv} + ik_{yv})^{m+\frac{1}{2}}}{k^{m+\frac{1}{2}}} + \delta_{v0} \right|^2 \quad (11)$$

where d is the separation between adjacent QDs, k_{xv} and k_{yv} respectively denote the propagation constants in the x and y directions with $k_{xv} = k_x + 2\pi v/d$, $k_{yv} = \sqrt{k^2 - k_{xv}^2}$ for $k^2 \geq k_{xv}^2$.

DATA AVAILABILITY

The data supporting the findings of this work are available from the corresponding authors upon reasonable request.

CODE AVAILABILITY

The related codes are available from the authors upon reasonable request.

Received: 26 August 2020; Accepted: 19 March 2021;

Published online: 16 April 2021

REFERENCES

- Geim, A. K. & Novoselov, K. S. The rise of graphene. *Nat. Mater.* **6**, 183 (2007).
- Bøggild, P. et al. A two-dimensional Dirac fermion microscope. *Nat. Commun.* **8**, 15783 (2017).
- Brandimarte, P. et al. A tunable electronic beam splitter realized with crossed graphene nanoribbons. *J. Chem. Phys.* **146**, 199902 (2017).
- Barnard, A. W. et al. Absorptive pinhole collimators for ballistic Dirac fermions in graphene. *Nat. Commun.* **8**, 15418 (2017).
- Rickhaus, P. et al. Guiding of electrons in a few-mode ballistic graphene channel. *Nano Lett.* **15**, 5819–5825 (2015).
- Kim, M. et al. Valley-symmetry-preserved transport in ballistic graphene with gate-defined carrier guiding. *Nat. Phys.* **12**, 1022 (2016).
- Cheng, A., Taniguchi, T., Watanabe, K., Kim, P. & Pillet, J.-D. Guiding Dirac fermions in graphene with a carbon nanotube. *Phys. Rev. Lett.* **123**, 216804 (2019).
- Li, J. et al. A valley valve and electron beam splitter. *Science* **362**, 1149–1152 (2018).
- Lin, Y.-M. et al. Wafer-scale graphene integrated circuit. *Science* **332**, 1294–1297 (2011).
- Shytov, A. V., Rudner, M. S. & Levitov, L. S. Klein backscattering and Fabry–Prot interference in graphene heterojunctions. *Phys. Rev. Lett.* **101**, 156804 (2008).
- Park, C.-H. et al. Electron beam supercollimation in graphene superlattices. *Nano Lett.* **8**, 2920–2924 (2008).
- Ren, Y. et al. Effective medium theory for electron waves in a gate-defined quantum dot array in graphene. *Phys. Rev. B* **100**, 045422 (2019).
- Young, A. F. & Kim, P. Quantum interference and Klein tunnelling in graphene heterojunctions. *Nat. Phys.* **5**, 222–226 (2009).
- Williams, J. R., Low, T., Lundstrom, M. S. & Marcus, C. M. Gate-controlled guiding of electrons in graphene. *Nat. Nanotechnol.* **6**, 222–225 (2011).
- Smith, D. R., Pendry, J. B. & Wiltshire, M. C. K. Metamaterials and negative refractive index. *Science* **305**, 788 (2004).
- Yu, N. & Capasso, F. Flat optics with designer metasurfaces. *Nat. Mater.* **13**, 139–150 (2014).
- Du, J. J. et al. Optical beam steering based on the symmetry of resonant modes of nanoparticles. *Phys. Rev. Lett.* **106**, 203903 (2011).
- Wu, A. et al. Negative-angle refraction with an array of silicon nanoposts. *Nano Lett.* **15**, 2055 (2015).
- Sell, D., Yang, J., Doshay, S., Yang, R. & Fan, J. A. Large-angle, multifunctional metagratings based on freeform multimode geometries. *Nano Lett.* **17**, 3752–3757 (2017).
- Cheianov, V. V., Fal'ko, V. & Altshuler, B. L. The focusing of electron flow and a Veselago lens in graphene pn junctions. *Science* **315**, 1252–1255 (2007).
- Chen, S. et al. Electron optics with p-n junctions in ballistic graphene. *Science* **353**, 1522–1525 (2016).
- Brun, B. et al. Imaging Dirac fermions flow through a circular Veselago lens. *Phys. Rev. B* **100**, 041401(R) (2019).
- Du, J. J., Lin, Z. F., Chui, S. T., Dong, G. J. & Zhang, W. P. Nearly total omnidirectional reflection by a single layer of nanorods. *Phys. Rev. Lett.* **110**, 163902 (2013).
- Pors, A., Nielsen, M. G. & Bozhevolnyi, S. I. Plasmonic metagratings for simultaneous determination of Stokes parameters. *Optica* **2**, 716–723 (2015).
- Fan, Z. et al. Perfect diffraction with multiresonant bianisotropic metagratings. *ACS Photon.* **5**, 4303–4311 (2018).
- Shi, T. et al. All-dielectric kissing-dimer metagratings for asymmetric high diffraction. *Adv. Opt. Mater.* **7**, 1901389 (2019).
- Cao, X. et al. Electric symmetric dipole modes enabling retroreflection from an array consisting of homogeneous isotropic linear dielectric rods. *Adv. Opt. Mater.* **8**, 2000452 (2020).
- Deng, Z. L. et al. Facile metagrating holograms with broadband and extreme angle tolerance. *Light Sci. Appl.* **7**, 78 (2018).
- Wan, W. et al. Holographic sampling display based on metagratings. *iScience* **23**, 100773 (2020).
- Katsnelson, M. I., Novoselov, K. S. & Geim, A. K. Chiral tunnelling and the Klein paradox in graphene. *Nat. Phys.* **2**, 620–625 (2006).
- Son, Y.-W., Cohen, M. L. & Louie, S. G. Energy gaps in graphene nanoribbons. *Phys. Rev. Lett.* **97**, 216803 (2006).
- Sofo, J. O., Chaudhari, A. S. & Barber, G. D. Graphane: a two-dimensional hydrocarbon. *Phys. Rev. B* **75**, 153401 (2007).
- Martinazzo, R., Casolo, S. & Tantardini, G. F. Symmetry-induced band-gap opening in graphene superlattices. *Phys. Rev. B* **81**, 245420 (2010).
- Naumov, I. I. & Bratkovsky, A. M. Gap opening in graphene by simple periodic inhomogeneous strain. *Phys. Rev. B* **84**, 245444 (2011).

35. Zhou, S. Y. et al. Substrate-induced bandgap opening in epitaxial graphene. *Nat. Mater.* **6**, 770–775 (2007).
36. Amet, F., Williams, J. R., Watanabe, K., Taniguchi, T. & Goldhaber-Gordon, D. Insulating behavior at the neutrality point in single-layer graphene. *Phys. Rev. Lett.* **110**, 216601 (2013).
37. Areshkin, D. A. & White, C. T. Building blocks for integrated graphene circuits. *Nano Lett.* **7**, 3253–3259 (2007).
38. Zhao, Y. et al. Creating and probing electron whispering-gallery modes in graphene. *Science* **348**, 672–675 (2015).
39. Jiang, Y. et al. Tuning a circular p-n junction in graphene from quantum confinement to optical guiding. *Nat. Nanotech.* **12**, 1045–1049 (2017).
40. Gutierrez, C., Brown, L., Kim, C.-J., Park, J. & Pasupathy, A. N. Klein tunnelling and electron trapping in nanometre-scale graphene quantum dots. *Nat. Phys.* **12**, 1069–1075 (2016).
41. Ghahari, F. et al. An on/off Berry phase switch in circular graphene resonators. *Science* **356**, 845–849 (2017).
42. Bai, K.-K. et al. Generating atomically sharp p-n junctions in graphene and testing quantum electron optics on the nanoscale. *Phys. Rev. B* **97**, 045413 (2018).
43. Matulis, A. & Peeters, F. M. Quasibound states of quantum dots in single and bilayer graphene. *Phys. Rev. B* **77**, 115423 (2008).
44. Hewageegana, P. & Apalkov, V. Electron localization in graphene quantum dots. *Phys. Rev. B* **77**, 245426 (2008).
45. Bardarson, J. H., Titov, M. & Brouwer, P. W. Electrostatic confinement of electrons in an integrable graphene quantum dot. *Phys. Rev. Lett.* **102**, 226803 (2009).
46. Heinisch, R. L., Bronold, F. X. & Fehske, H. Mie scattering analog in graphene: lensing, particle confinement, and depletion of Klein tunneling. *Phys. Rev. B* **87**, 155409 (2013).
47. Katsnelson, M. I., Guinea, F. & Geim, A. K. Scattering of electrons in graphene by clusters of impurities. *Phys. Rev. B* **79**, 195426 (2009).
48. Ostrovsky, P. M., Gornyi, I. V. & Mirlin, A. D. Electron transport in disordered graphene. *Phys. Rev. B* **74**, 235443 (2006).
49. Hentschel, M. & Guinea, F. Orthogonality catastrophe and kondo effect in graphene. *Phys. Rev. B* **76**, 115407 (2007).
50. Novikov, D. S. Elastic scattering theory and transport in graphene. *Phys. Rev. B* **76**, 245435 (2007).
51. Pieper, A., Heinisch, R. L. & Fehske, H. Scattering of two-dimensional Dirac fermions on gate-defined oscillating quantum dots. *Phys. Rev. B* **91**, 045130 (2015).
52. Cserti, J., Pályi, A. & Péterfalvi, C. Caustics due to a negative refractive index in circular graphene P-N junction. *Phys. Rev. Lett.* **99**, 246801 (2007).
53. Pieper, A., Heinisch, R. L. & Fehske, H. Electron dynamics in graphene with gate-defined quantum dots. *Europhys. Lett.* **104**, 47010 (2013).
54. Caridad, J. M., Connaughton, S., Ott, C., Weber, H. B. & Krstić, V. An electrical analogy to Mie scattering. *Nat. Commun.* **7**, 12894 (2016).
55. Tang, Y. et al. Flat-lens focusing of electron beams in graphene. *Sci. Rep.* **6**, 33522 (2016).
56. Bai, K.-K. et al. Generating atomically sharp p-n junctions in graphene and testing quantum electron optics on the nanoscale. *Phys. Rev. B* **97**, 045413 (2018).
57. Gutiérrez, C., Brown, L., Kim, C.-J., Park, J. & Pasupathy, A. N. Klein tunnelling and electron trapping in nanometre-scale graphene quantum dots. *Nat. Phys.* **12**, 1069–1075 (2016).
58. Bai, K.-K., Qiao, J.-B., Jiang, H., Liu, H. & He, L. Massless Dirac fermions trapping in a quasi-one-dimensional npn junction of a continuous graphene monolayer. *Phys. Rev. B* **95**, 201406(R) (2017).
59. Korringa, J. On the calculation of the energy of a Bloch wave in a metal. *Physica* **13**, 392–400 (1947).
60. Kohn, W. & Rostoker, N. Solution of the Schrodinger equation in periodic lattices with an application to metallic lithium. *Phys. Rev.* **94**, 1111 (1954).

ACKNOWLEDGEMENTS

This work was supported by NNSFC (Grant no. 11474098).

AUTHOR CONTRIBUTIONS

J.D. conceived the concept. P.W., Y.R. and J.D. performed theoretical and numerical calculations. Q.W., D.H., L.Z., and H.G. contributed insight and discussion on the results. P.W. and J.D. wrote the paper. J.D. supervised the project.

COMPETING INTERESTS

The authors declare no competing interests.

ADDITIONAL INFORMATION

Supplementary information The online version contains supplementary material available at <https://doi.org/10.1038/s41699-021-00222-3>.

Correspondence and requests for materials should be addressed to J.D.

Reprints and permission information is available at <http://www.nature.com/reprints>

Publisher's note Springer Nature remains neutral with regard to jurisdictional claims in published maps and institutional affiliations.



Open Access This article is licensed under a Creative Commons Attribution 4.0 International License, which permits use, sharing, adaptation, distribution and reproduction in any medium or format, as long as you give appropriate credit to the original author(s) and the source, provide a link to the Creative Commons license, and indicate if changes were made. The images or other third party material in this article are included in the article's Creative Commons license, unless indicated otherwise in a credit line to the material. If material is not included in the article's Creative Commons license and your intended use is not permitted by statutory regulation or exceeds the permitted use, you will need to obtain permission directly from the copyright holder. To view a copy of this license, visit <http://creativecommons.org/licenses/by/4.0/>.

© The Author(s) 2021